Experimental investigation on the influence of gap vortex streets on fluid-structure interactions in hexagonal bundle geometries

Bertocchi, F.; Rohde, M.; Kloosterman, J. L.

DOI
10.1016/j.ijheatfluidflow.2019.108443

Publication date
2019

Document Version
Final published version

Published in
International Journal of Heat and Fluid Flow

International Journal of Heat and Fluid Flow 79 (2019) 108443

Contents lists available at ScienceDirect

International Journal of Heat and Fluid Flow

journal homepage: www.elsevier.com/locate/ijhff

Experimental investigation on the influence of gap vortex streets on fluid-structure interactions in hexagonal bundle geometries

F. Bertocchi*, M. Rohde, J.L. Kloosterman

Department of Radiation Science and Technology, Delft University of Technology, Mekelweg 15, Delft, 2629 JB, the Netherlands

ARTICLE INFO

Keywords:
Coherent structures
Rod bundle
Fluid-structure interactions
Laser Doppler Anemometry

ABSTRACT

Gap vortex streets characterise many industrial applications involving rod bundle flows, such as heat exchangers and nuclear reactors. These structures, known as gap vortex streets, may excite the structural components of the bundle to resonance, leading to fretting and fatigue. This work aims to measure these coherent structures and the resulting displacement and oscillation frequency of the neighbouring rod, to provide unique data for fluid-structure interaction studies and to develop a general correlation for estimating the coherent structure's wavelength. A water loop was built to host a hexagonal rod bundle. Fluorinated Ethylene Prophylene (FEP), a refractive index matching (RIM) material, was used to have undisturbed optical access in the area around the central rod. The flow was measured with Laser Doppler Anemometry (LDA) to detect coherent structures, while the vibrations were measured with a high speed camera. A new correlation for estimating the wavelength of the coherent structures is derived with dimensional analysis based on experimental evidence. The correlation is tested on different geometries: rectangular channels with single or half-rods, and two rod bundles, within the pitch-to-diameter ratio (P/D) range 1.02–1.2. Moreover fluctuations in the flow, given by the detected coherent structures, govern the structural response of the rod. The rod is excited to resonance if these fluctuations match twice the natural frequency of the rod.

Nomenclature

Latin symbol	Description	Dimension
A	Flow area	m^2
C_m	Added mass coefficient	-
C_N	Lateral drag force coefficient	-
C_T	Longitudinal viscous force coefficient	-
C_V	Viscous damping coefficient	-
C'_{fT}, $C'_{fT,c}$, $C'_{fT,e}$	Coefficient for pressure drops	-
D	Rod diameter	m
D_h, D_h^*, $D_{h,c}$, $D_{h,e}$	Gap hydraulic diameter	m
D_o	Equivalent diameter	m
$D_{sil,i}$	Inner silicone rod diameter	m
E	Young modulus	Pa
f_{str}	Frequency of the coherent structures	Hz
f_{wall}	Frequency of vibration of the silicone rod edge	Hz
f^*	Non dimensional frequency	-

Abbreviations: CMOS, Complementary Metal-Oxide Semiconductor; fps, Frames per second; FEP, Fluorinated Ethylene Propylene; FIV, Flow-Induced Vibration; FFT, Fast Fourier Transform; FSI, Fluid-Structure Interaction; PMMA, Polymethyl Methacrylate; LDA, Laser Doppler Anemometry; MP, Mega pixel; NRMSE, Normalised r.m.s. Error; RIM, Refractive Index Matching; 2D, 3D, Two/Three dimensional; **Subscript**, **Description**; c, Pertaining to the central sub-channel; e, Pertaining to the edge sub-channel; gap, Pertaining to the gap region; wall, Pertaining to the rod's vibrations; str, Pertaining to the coherent structures; in, Stream-wise velocity profile inflection point; min, Lower limit of flow structure lengths; Max, Upper limit of flow structure lengths

* Corresponding author.
E-mail address: F.Bertocchi@tudelft.nl (F. Bertocchi).

https://doi.org/10.1016/j.ijheatfluidflow.2019.108443
Received 22 February 2019; Received in revised form 16 May 2019; Accepted 10 July 2019
Available online 22 August 2019
0142-727X/

f_c, f_e	Friction factor	-
I	Moment of inertia of the silicone rod	m^4
L_{dev}	Development length	m
L_{fl}	Flexible (silicone) rod length	m
l	Rod length	m
$\dot{m}$	Mass flow rate	$kg\,s^{-1}$
m	Rod mass	$kg\,m^{-1}$
m_a	Added mass	$kg\,m^{-1}$
N	Number of recorded positions of the silicone rod edge	-
N_s	Number of fitted points of the spectrum	-
n	Friction factor coefficient	-
P/D	Pitch-to-diameter ratio	-
P	Random pressure field	Pa
S	Strain rate tensor	s^{-1}
S	Frequency spectrum	s
t	Time	s
t_{FEP}	FEP wall thickness	m
t_{sil}	Silicone thickness	m
U	Mean streamwise velocity near the silicone rod	$m\,s^{-1}$
v	Stream-wise velocity component	$m\,s^{-1}$
v_{gap}	Mean velocity in the gap region	$m\,s^{-1}$
v_{in}	Inflection point's velocity	$m\,s^{-1}$
v^*	Non dimensional velocity	-
W/D	Wall-to-rod ratio	-
x, z	Span-wise and stream-wise coordinates	m
x_{fit}, x_s	Fitted and measured value of the spectrum	s

Non dimensional number	**Description**
Re, Re_{gap}, Re_c, Re_e	Reynolds number

Greek symbol	**Description**	**Dimension**
α	Flow conveyer's divergence angle	°
β, ξ, γ	Coefficients	-
λ	Flow structure length	m
$\delta\lambda$	Wavelength uncertainty	m
Δp, Δp_{gap}	Pressure drop	Pa
Δp_c, Δp_e	Pressure drop	Pa
$\bar{\varepsilon}$	Vibration amplitude	m
$\bar{\varepsilon}_{rms}$	Vibration amplitude r.m.s.	m
μ	Dynamic viscosity	$Pa\,s^{-1}$
ρ	Density	$kg\,m^{-3}$
σ	Okubo-Weiss criterion's parameter	s^{-1}
Ω_n	Non dimensional silicone rod natural frequency	-
ω	Vorticity	s^{-1}
$\mathcal{K}$, $\mathcal{K}'$	Constant	-

1. Introduction

Rod bundle flows are common in industrial applications, such as heat exchangers or conventional and next generation nuclear reactors. The core of a nuclear power plant consists of slender pins hosting the nuclear fuel, which are clustered together in a lattice defined by the pitch-to-diameter ratio (P/D), and by the arrangement, either hexagonal or squared. The coupling of such geometries with an axial flow of coolant to remove the generated heat constitutes a rod bundle flow. The presence of an axial flow of fluid through a rod bundle leads to velocity differences between the low-speed region of the gap between two rods, and the high-speed region of the main sub-channels. This velocity difference produces a shear layer between the two flow regions, leading to streaks of vortices carried by the current. Generally those vortices (or flow structures) occur on both sides of the gap enclosed by two adjacent rods, identifying the so-called *gapvortex streets* (Tavoularis, 2011), or large coherent structures.

The formation mechanism of the gap vortex streets is akin to the Kelvin-Helmholtz instability arising between two parallel layers of fluid moving with different speeds (Meyer, 2010). An inflection point in the stream-wise velocity profile is a necessary condition (though not sufficient) to have these coherent structures, as predicted by the Rayleigh's instability criterion (Rayleigh, 1879). Unlike free mixing layers, vortex streets are stable along the flow, hence the adjective *coherent*. Furthermore, a lateral (span-wise) flow across the gap between the rods may also occur (cross-flow). In a nuclear reactor, cross-flow enhances lateral mixing between subchannels. The fuel temperature decreases accordingly, improving the safety performance of the reactor.

Fluid-structure interaction (FSI) between these coherent structures and the rods causes flow-induced vibrations (FIV) on the structural components, leading to damage by fretting (Païdoussis, 1981). If coherent structures have a length comparable in magnitude with the axial dimension of the rod assembly, they may cause resonance in the first and most energetic mode. Conversely, the presence of multiple, shorter coherent structures on either side of the rod would diminish their effect on the most energetic mode and may cause oscillations at higher, less energetic modes. However, coherent structures shorter than the rod might still cause oscillations at higher modes.

Research has widely covered the topic of coherent structures in rod bundles, both experimentally and numerically. Rowe measured coherent flow structures through a gap where the P/D was adjustable to 1.125 and to 1.250 (Rowe et al., 1974). Rehme proposed a static pressure instability mechanism to account for the formation of coherent structures (Rehme, 1987). Möller adopted the term *metastableequilibrium* to picture the

instantaneous difference in velocity and vorticity near the gap (Möller, 1991). Gosset and Tavoularis (2006) and Piot and Tavoularis (2011) investigated the lateral mass transfer across an eccentric annular gap with flow visualization techniques. Mahmood studied coherent structures in a square rod bundle over a range of Reynolds number (Mahmood, 2011). Later, Choueiri and Tavoularis studied the flow instability through the gap in the same geometry (Choueiri and Tavoularis, 2014; 2015). They found that the velocity fluctuations along the span-wise direction in the centre of the gap, compared to those in the axial direction, were varying in time with a rate twice as slow. This was consistent with the model previously proposed by Meyer and Rehme (1994). Chang and Tavoularis (2005), and Merzari conducted numerical studies on the same geometry (Merzari and Ninokata, 2011). Baratto investigated the air flow inside a 5-rods model of a CANDU fuel bundle (Baratto et al., 2006). FIV have also been thoroughly studied (Païdoussis, 1966; 1974). Recently Paidoussis enriched the literature on the subject with a two-volumes handbook (Païdoussis, 2014; 2016), collecting together most of the knowledge. Although there is abundance of FSI studies on both solitary cylinders or cluster of rods in axial flows, an experimental study of the role that coherent structures play in FSI inside rod bundles is missing. Furthermore, a tool for estimating the length of the coherent structures applicable to different geometries would contribute to designing safer components not subject to resonance. The approach is twofold: providing a new general correlation to estimate the size of the structures in different channel geometries and characterising the response frequency of the vibrating rod as a function of the rate of passage of the coherent structures. The measurement systems that are employed are Laser Doppler Anemometry (LDA) and a high-speed camera. The experimental setup consists of a 7-rods hexagonal bundle where part of the central rod consists of flexible silicone, which has previously been employed for other FIV studies (Modarres-Sadeghi et al., 2008). Optical access to the measurement region without light distortion is achieved through the refractive index matching technique (RIM). This has become a widely used solution for performing optical measurements in rod bundles. Dominguez followed such a method for his measurements inside a 3×3 and 5×5 square rod bundle (Dominguez-Ontiveros and Hassan, 2009; Dominguez-Ontiveros and Hassin, 2014). More recently experiments performed at Texas University made use of the RIM technique with a larger 61-pins hexagonal bundle (Nguyen et al., 2017; Nguyen and Hassan, 2017). In this work, part of the outer rods of the assembly are made of Fluorinated Ethylene Propylene (FEP), which matches the refractive index of water (Mahmood, 2011). FEP is one of the refractive-index matching materials, together with Mexflon-DC employed by Sato et al. (2009), commonly used for this kind of applications (Hosokawa et al., 2012; Bertocchi et al., 2018). LDA measurements of the flow field are done to characterise the vortex streets in the considered geometry, followed by a measurement campaign with the high-speed camera to detect flow-induced vibration of the rod. The small size of this work's bundle allows for an easier optical access around the central rod, which is crucial for measuring vibrations.

2. Theory

2.1. Natural frequency of a rod

Estimating the natural frequency of the silicone rod is required to interpret the results of the FSI measurement campaign. The Euler–Bernoulli beam theory for a single cylinder clamped at both ends, immersed in a steady, axial flow, and surrounded by an outer channel, gives the equation derived by Païdoussis (1966):

$$EI\frac{\partial^4 x}{\partial z^4} + m_a\left(U^2\frac{\partial^2 x}{\partial z^2} + \frac{\partial^2 x}{\partial t^2}\right) - \frac{1}{2}C_T\frac{m_a U^2}{D}\left(\frac{1}{2}l - z\right)\frac{\partial^2 x}{\partial z^2} + 2m_a U\frac{\partial^2 x}{\partial z \partial t} + + \frac{1}{2}C_N\frac{m_a U}{D}\left(U\frac{\partial x}{\partial z} + \frac{\partial x}{\partial t}\right) + C_V\frac{\partial x}{\partial t} + m\frac{\partial^2 x}{\partial t^2} = 0 \quad (1)$$

where E is Young's modulus of the silicone (typically 1 MPa), I is the moment of inertia of the silicone rod evaluated as $I = \frac{\pi}{4}(D^2/4 - D_{sil,i}{}^2/4)$, being $D_{sil,i}$ the inner diameter of the silicone rod.

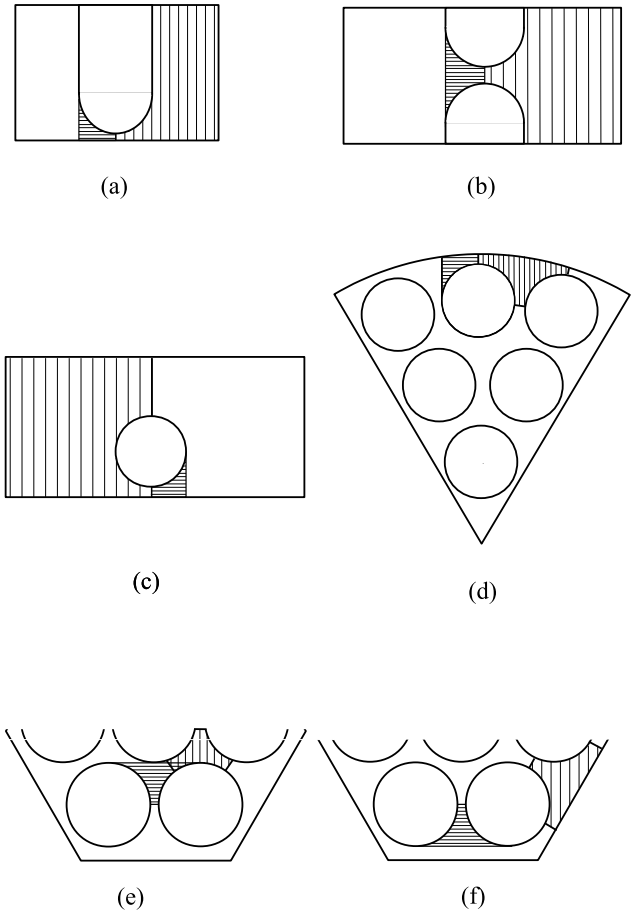

Fig. 1. Definition of the hydraulic diameters of the gap region for the bundle geometries considered to test the correlation. (a) Adopted from Mahmood (2011). (b) Adopted from Bertocchi et al. (2018). (c) Adopted from Guellouz and Tavoularis (2000). (d) Adopted from Don and Tavoularis (2018). (e–f) This work. Horizontal hatching: gap region. Vertical hatching: main subchannel. For clarity, the main subchannel and the gap region are drawn as two separate regions whereas, in the reality, they partly overlap.

x is the rod radial displacement, z is the axial coordinate along the rod, m_a is the added mass accounting for the additional force exerted by the fluid on the rod while it moves, U is the mean axial flow velocity, C_T is the longitudinal viscous force coefficient whose definition is given in Hoerner (1965), D is the rod diameter, l is the rod length, $C_N = C_T$ is the lateral drag force coefficient, C_V is the viscous damping coefficient (Sinyavskii et al., 1980), and m is the rod mass. The added mass m_a deserves a more detailed treatment since it accounts for the confinement effect given by the proximity of other bodies (i.e. walls, rods) around the silicone rod. The added mass is defined as

$$m_a = C_m \cdot \rho\pi\frac{D^2}{4}, \quad (2)$$

where the C_m is the added mass coefficient which multiplies the weight of the fluid displaced by the rod in the flow. It represents the confinement effect of an outer channel surrounding a single rod (Sinyavskii et al., 1980; Païdoussis, 2014; Pettigrew and Taylor, 1994). Although C_m is a function of the outer channel diameter D_o, the central rod of the bundle is actually surrounded by multiple rods, and not by a larger concentric tube. Therefore, D_o must be adapted to the rod bundle case by defining an equivalent hydraulic diameter given by the flow area of the surrounding six subchannels. The natural frequency Ω_n of the central silicone rod is obtained with the procedure described in Païdoussis (2014) and Chen (1985), where the equation is first non-dimensionalised and then solved by the Galerkin method.

2.2. Empirical correlation for the length of coherent structures in bundle geometries

Estimating the wavelength of coherent structures is important for designing experiments that aim at studying specific sizes of the structures in rod bundles. The needed expression should be applicable to different geometries of the subchannels of a rod bundle. Therefore, an empirical correlation for estimating the wavelength λ of the structures is derived based on dimensional analysis. The wavelength λ is assumed to depend on the local channel geometry (hydraulic diameter of the main subchannel and of the gap region) and fluid properties. The flow velocity in the gap and in the main subchannel are also considered as parameters that determine the length of the structures (Mahmood, 2011). In mathematical terms,

$$\lambda = \mathcal{K}\cdot(D_h^*)^a\cdot\rho^c\cdot\mu^d\cdot v^e\cdot v_{gap}^f\cdot D_h^g, \tag{3}$$

where $\mathcal{K}$ is an arbitrary constant, D_h^* is the hydraulic diameter of the gap region (defined in Fig. 1), ρ is the fluid density, μ is the dynamic viscosity, and v is the fluid velocity in the main subchannel, v_{gap} is the fluid velocity in the gap region, and D_h is the hydraulic diameter of the main subchannel.

From dimensional analysis, it follows that

$$\frac{\lambda}{D_h} = \mathcal{K}\cdot\left(\frac{D_h^*}{D_h}\right)^a Re^c \left(\frac{v_{gap}}{v}\right)^f. \tag{4}$$

At high Reynolds numbers it is reasonable to assume that the pressure drops across the gap region Δp_{gap} and across the main subchannel Δp, over a length L, are the same:

$$\Delta p_{gap} = \frac{\rho}{2}v_{gap}^2\frac{L}{D_h^*}f(Re_{gap}) = \Delta p = \frac{\rho}{2}v^2\frac{L}{D_h}f(Re), \tag{5}$$

where $f(Re) = C_1 Re^{-b_1}$ and $f(Re_{gap}) = C_2 Re_{gap}^{-b_2}$ (Todreas and Kazimi, 1990). The ratio v_{gap}/v is then expressed by

$$\frac{v_{gap}}{v} = \left[\frac{f(Re_{gap})}{f(Re)}\frac{D_h^*}{D_h}\right]^{1/2}. \tag{6}$$

Substituting Eq. (6) into Eq. (4) leads to

$$\frac{\lambda}{D_h^*} = \mathcal{K}'\left(\frac{D_h^*}{D_h}\right)^\xi Re^c f(Re) f(Re_{gap}). \tag{7}$$

Experimental evidence has shown that the wavelength is independent on the Reynolds number of the main subchannel Re (Bertocchi et al., 2018; Mahmood, 2011; Guellouz and Tavoularis, 2000; Meyer and Rehme, 1995), so

$$\frac{\lambda}{D_h^*} = \mathcal{K}'\left(\frac{D_h^*}{D_h}\right)^\xi Re_{gap}^\gamma. \tag{8}$$

The correlation will be tested against the experiments performed in simple geometries such as rectangular channels hosting respectively one or two half-rods (Mahmood, 2011; Bertocchi et al., 2018), and an eccentric rod hosted in a rectangular channel (Guellouz and Tavoularis, 2000). Furthermore, two rod bundle geometries are considered: the hexagonal bundle of this work and a sector of a circular bundle (Don and Tavoularis, 2018). The results of the validation with the experiments is discussed in Section 5.2.1.

2.3. Oscillating pressure field

The Weiss–Okubo criterion (Weiss, 1991; Okubo, 1970) states that coherent structures occur in vorticity-dominant regions of the flow in which $\sigma^2 < 0$, being

$$\sigma^2 = tr\mathbf{S^2} - \omega^2, \tag{9}$$

where $tr\mathbf{S^2}$ is the trace of the strain rate tensor $\mathbf{S^2}$, and ω is the vorticity.

Table 1
Bundle's main dimensions. D: outer rod diameter, P/D: pitch-to-rod diameter ratio, W/D: wall-to-rod diameter ratio, t_{sil}: wall thickness of the silicone rubber tube, α: half-aperture angle of the flow distributor, L_{dev}: development length upstream of the optical window, t_{FEP}: FEP wall thickness, L_{fl}: silicone rubber tube length (including sections slid over the rods).

Bundle geometry	Design parameters
D = 30mm	t_{sil} = 1.5mm
P/D = 1.11	α = 4°
W/D = 1.11	L_{dev} = 1500mm
	t_{FEP} = 0.25mm
	L_{fl} = 100mm + 2 × 45mm

Moreover, considering a pressure field P, the relation (Larchevêque, 1993)

$$\nabla^2 P = -\frac{1}{2}\sigma^2 \tag{10}$$

indicates that coherent structures occur where $\nabla^2 P > 0$, that is a low-pressure region of the flow dominated by vorticity (Métais and Lesieur, 1992). Hence, coherent structures moving along the rod result in an oscillating pressure field moving with the flow that imposes a fluctuating force on the wall.

3. Experimental setup

3.1. Test loop

The experimental apparatus consists of a water loop with a 7-rods hexagonal bundle, where the central rod has a section made of flexible silicone rubber. The rod bundle is enclosed inside an outer hexagonal encasing of transparent polymethyl methacrylate (PMMA). The water flows top-down by gravity from an upper vessel through the bundle and is collected in a lower tank, where it is recirculated by a centrifugal pump towards the upper vessel. A valve with a linear response is located in the downcomer pipe to control the flow rate, which is monitored by a magnetic flow meter (ABB - type HA3).

3.2. Bundle geometry

In order to have vibrations induced by coherent structures, the silicone rod length must be comparable to the size of the expected coherent structures. If the rod is too long compared to the size of the coherent structures, the effects of the structures would cancel out and no flow-induced oscillation would be measurable. A study from Gent University (Ridder et al., 2016), done with the same P/D ratio, showed that coherent structures were expected to have a length of 7 cm. The length of the silicone section is set to 10 cm accordingly. The main parameters of the hexagonal lattice and of the test section are listed in Table 1.

The sketch of the optical window, of the inlet flow distributor, and of the whole test section are provided in Fig. 2. The flow enters from the top and the water is distributed over the 18 subchannels via the flow distributor (Fig. 2b); after a development length L_{dev} of 1.5m, the flow reaches the location of the measurement section (Fig. 2c, detail B). The internal structure of the flow distributor disrupts the large eddies that may be present in the stream, and it redistributes the flow uniformly among the subchannels of the bundle. Flow detachment from its walls is avoided by adopting a divergent angle of 4° (Idel'chik, 1966).

Optical access for the measurement systems around the central rod is achieved by partially replacing the stainless steel of the front rods with FEP, heat-shrunk around the body (Figs. 3a, b). The total length of the FEP tube is 190mm, of which 100mm provide the transparent

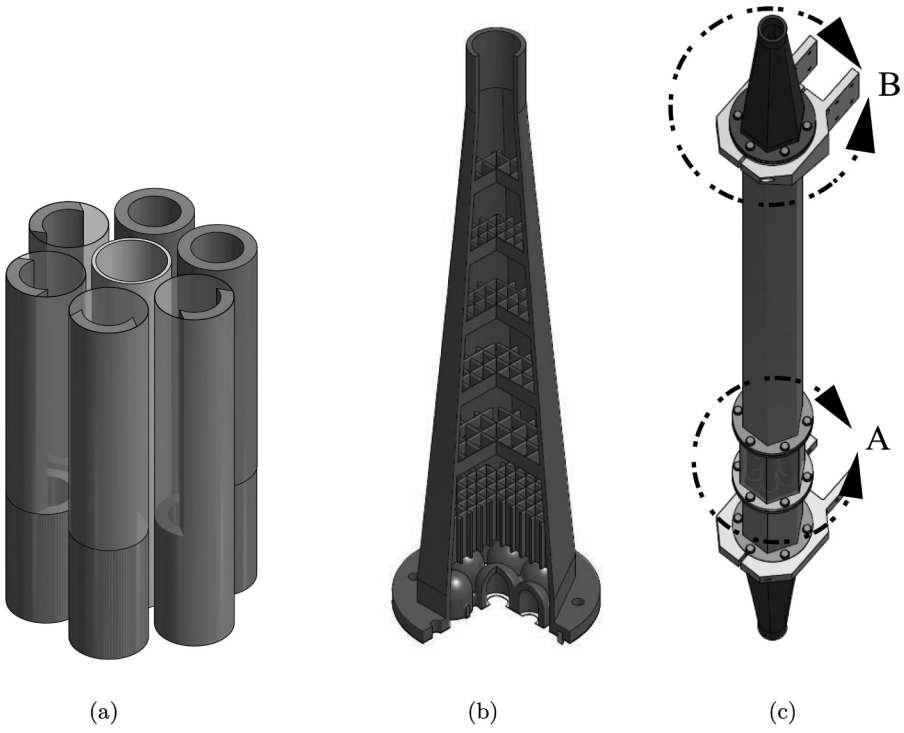

Fig. 2. (a) Sketch of the bare rod bundle with enlarged measurement section where the FEP rods are visible. The flow direction is from top to bottom. (b) The inlet flow distributor has an internal structure of fins to break the large eddies in the flow. (c) Rod bundle test section enclosed inside the hexagonal casing; (detail A) transparent measurement section, (detail B) inlet flow conveyer.

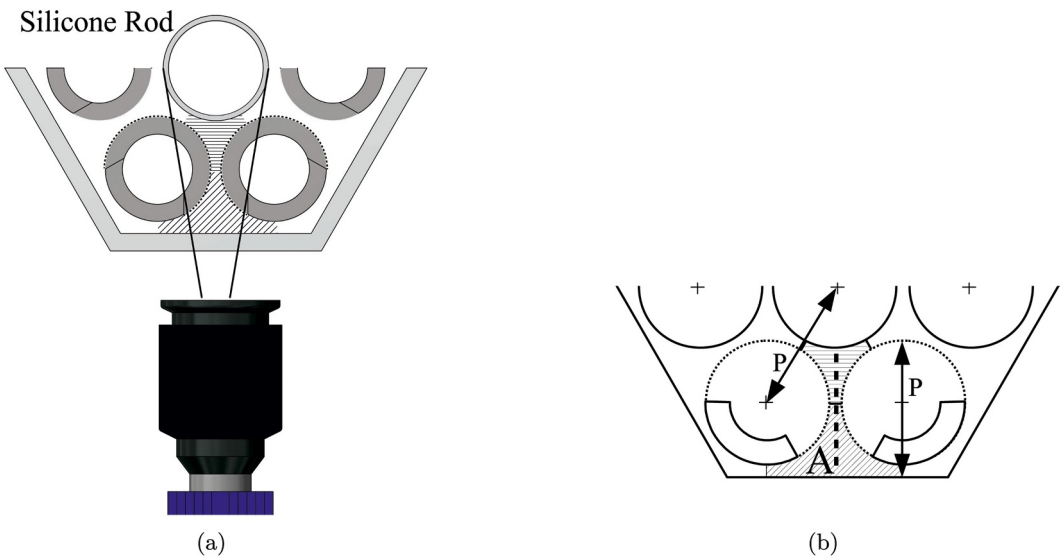

Fig. 3. (a) FIV tracking system for recording the position of one border of the rod. (b) Top view of half of the hexagonal bundle geometry. The dashed profile on the rods represents the FEP replacing the steel; the straight hatched line A represents the LDA measurements positions. The rods are filled with water to avoid image distortion through FEP. Horizontal hatching: central subchannel. Diagonal hatching: edge subchannel.

window for the measurements. The FEP tube is shrunk around the steel rod for a length of 45mm at both the extremities. The outer radius of the metal rod is reduced by the FEP wall thickness (t_{FEP} = 0.25mm), hence there is no step in the transition between stainless steel and FEP that might affect the flow.

4. Measurement apparatus

4.1. LDA system

The first measurement system to be used is a 2-component LDA system (DANTEC, Denmark) with a maximum power of 300mW. The measurement settings are adjusted via the BSA Flow Software (DANTEC, Denmark). The flow is seeded with particles to scatter the light once they travel through the sensitive region of the laser beam pair. This is an ellipsoidal probe of 0.02mm^3 (dx = dy = 79μ m; dz = 790μ m). Borosilicate glass hollow spheres (LaVision, Germany) with an average density of 1.1gcm^{-1} and a diameter of 9–12μ m are used. The LDA is moved in position with a traverse system.

4.2. LDA measurements

The Reynolds number of the subchannel, the wavelength of the coherent structures and the frequency of their passage are based on the measurements carried out with the LDA system. LDA measurements are conducted in the middle of the hexagonal transparent section, moving the laser probe from a position close to the outer wall towards the central rod, as shown in Fig. 3b. The 95% confidence level is evaluated

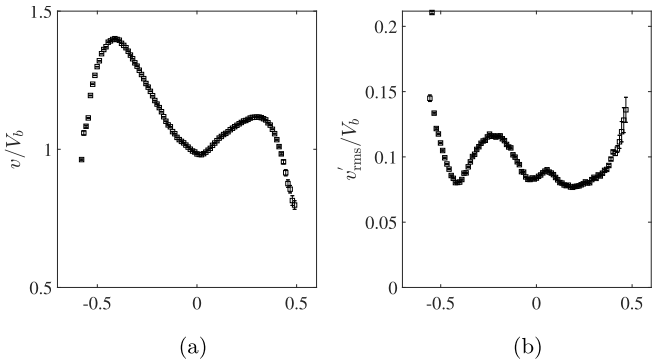

Fig. 4. Stream-wise velocity profile (a) and root mean square (b) measured with LDA through the gap between two front rods. The abscissa is the distance from the gap centre, normalized to the rod diameter.

for the mean stream-wise velocity: it is as low as 0.5% for all the measurement cases. A stopping criterion ends the measurements once 100000 samples are collected at each location. The flow rate is set within the range 1.05–4.80 kgs^{-1}. Two additional measurements close to the beginning and end of the transparent section help to check whether the flow structures are fully developed over its entire length. Fig. 4 shows the LDA measurement along the straight line throughout the gap between two front rods, with Re_e = 30540 (Re_c = 22940). The normalised stream-wise velocity component is reported in Fig. 4a. The velocity root mean square is shown in Fig. 4b, which features two maxima located at the outer wall and at close to the central rod, where turbulence increases due to the shear produced by the viscous sublayer, similarly to common wall-bounded flows (Pope, 2000). The relative maxima closer to the centre gap are due to the shear between the high-velocity region in the bulk and the low-velocity fluid inside the narrow gap (Bertocchi et al., 2018).

4.2.1. The slotting technique

The velocity samples measured by the LDA system are not evenly spaced in time, therefore a common Fast Fourier Transform (FFT) is not recommended. The spectra are, thus, evaluated by means of the slotting technique (Mayo, 1974; Tummers and Passchier, 2001; 1996), where sample pairs detected within a certain time interval (lag time) are allocated into the same *slot*. The product of the velocities of each sample pair (cross-product) is calculated and the average is taken within each slot. The slotting technique omits the cross-products with zero lag time (self-products), reducing the uncorrelated noise. The amount of particles crossing the probe volume is higher for high speed, biasing the spectrum at high frequencies (Adrian and Yao, 1986). Consequently, their contribution to the spectrum will be higher than the real one. Therefore, the transit time weighting algorithm is applied to the slotting technique to reduce this effect (Nobach, 2002). Once all the samples are allocated inside the slots, the autocorrelation coefficient is computed for each slot, and then the frequency spectrum is estimated. Periodical fluctuations of the fluid velocity given by coherent structures appear as a peak in the frequency spectrum.

4.2.2. Edge subchannel Reynolds number

The results of this work are collected with measurements performed inside the central subchannel and inside the edge subchannel. Therefore, it is more accurate to use the Reynolds of the edge and of the central subchannel, rather than estimating the Reynolds based on the total bundle flow area. The Reynolds number of the edge subchannel, Re_e, is estimated as follows:

$$Re_e = \frac{\rho \cdot v_e \cdot D_{h,e}}{\mu}, \tag{11}$$

where ρ and μ are the density and dynamic viscosity of water, respectively; $D_{h,e}$ is the hydraulic diameter of the edge subchannel ($4A/P_w$), and v_e is the average stream-wise velocity inside the edge subchannel. The latter is evaluated by measuring the velocity over the flow area A in the edge subchannel (Fig. 3b), and calculating the average according to

$$v_e = \frac{1}{A}\sum_i \sum_j v(x_i, y_j)\delta A_{ij}, \tag{12}$$

where δA_{ij} differs per position.

Table 2
Mass flow rate corresponding to the measured edge Reynolds number Re_e and to the estimated central subchannel's Reynolds number Re_c (Eq. (16)).

$\dot{m}$ [kgs^{-1}]	Re_e	Re_c
4.78	48 360	36 530
3.48	30 540	22 940
3.28	28 200	21 180
2.92	26 240	19 700
2.68	25 130	18 880
2.42	22 660	17 000
2.13	20 310	15 260
1.94	16 620	12 490
1.59	14 950	11 230
1.31	12 730	9 560
1.05	10 100	7 580

4.2.3. Central subchannel Reynolds number

The Reynolds number of the central subchannel, Re_c, is determined based on Re_e. Re_c requires the values of the average stream-wise velocity v_c in the central subchannel. The pressure drops along all subchannels may be considered to be the same, as in Todreas and Kazimi (1990), i.e. $\Delta p_e = \Delta p_c$. The velocity v_c can be obtained by using the Darcy-Weisbach equation (White, 2016):

$$\frac{f_c \rho v_c^2}{D_{h,c}} = \frac{f_e \rho v_e^2}{D_{h,e}}, \tag{13}$$

where $D_{h,c}$ is the hydraulic diameter of the central subchannel, f_c and f_e are the friction factors of central and edge subchannels, respectively. For a bare rod bundle (no spacers) in turbulent regime, f_c and f_e can be expressed as (Todreas and Kazimi, 1990)

$$f = \frac{C'_{fT}}{Re^n}, \tag{14}$$

where n = 0.18, and C'_{fT} is a coefficient depending on the hexagonal lattice. This correlation is valid for bare rod bundles within the pin number range of 7–217. Its mean error has been showed to be as low as 9 % (Chen et al., 2018). From Eqs. (13) and (14) it follows that

$$v_c = v_e \cdot \left[\frac{C'_{fT,e} D_{h,c}}{C'_{fT,c} D_{h,e}} \left(\frac{D_{h,c}}{D_{h,e}} \right)^n \right]^{\frac{1}{2-n}}. \tag{15}$$

Re_c is finally evaluated as

$$Re_c = \frac{\rho \cdot v_c \cdot D_{h,c}}{\mu}. \tag{16}$$

The values of Re_e and Re_c at which the LDA measurements are done, are reported in Table 2.

4.3. FIV tracking system

The equipment to measure flow-induced vibrations of the silicone rod consists of a Complementary Metal-Oxide Semiconductor (CMOS) camera Imager MX 4M (LaVision, Germany) capable of recording at 180 fps with full resolution (4 MP), and at 300 fps with a smaller field of view. The FIV tracking system cannot have both borders of the rod in

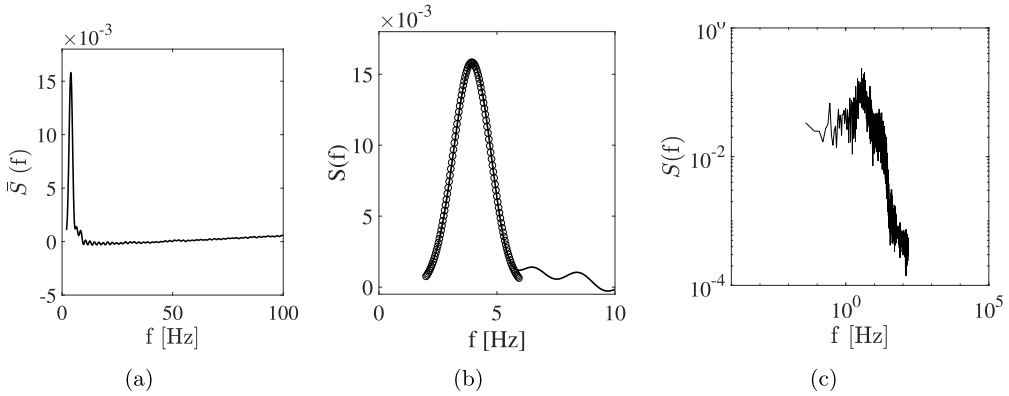

Fig. 5. (a) Example of frequency spectrum for the vibration of the silicone rod wall (Re_e= 23 660); the peak is located at 3.9Hz. (b) Gaussian fitting (circle) of the spectral peak (continuous line); (c) FFT frequency spectrum of the vibrating silicone rod.

focus with sufficient resolution because the camera should be moved too far from the target. Therefore the camera is focused on one border and records 15 000 images at 300 fps in each measurement. The Nyquist frequency, being the highest frequency of a signal that can be captured with a given sampling rate, is 150 fps. The frequency of the vibrating silicone rod is expected to be of the same order of the coherent structures' frequency, which is ≈ 10Hz based on preliminary LDA measurements. Hence, a recording rate of 300 fps is considered high enough to measure vibrations induced on the silicone rod. The contrast between the white silicone and the dark background is improved using a flash light to illuminate the target area, and by keeping the setup in the dark. A binary filter converts the intensity values of the light in the image into ones or zeros, according to the threshold level determined with the Otsu algorithm (Otsu, 1979). The location of the vertical border between the two regions of the filter represents the position of the silicone rod in the image. Each pair of consecutive silicone rod's positions is used to obtain the instantaneous displacement on the plane orthogonal to the line of sight of the camera (Fig. 3a). The series of instantaneous displacements gives the average displacement $\bar{\varepsilon}$, and the average root mean square $\bar{\varepsilon}_{\mathrm{rms}}$ (being dispersion of the displacement values around the mean, analogous to the standard deviation), which are calculated with Eq. (17).

$$\bar{\varepsilon} = \frac{1}{N-1}\sum_{i=1}^{N-1}\varepsilon_i; \qquad \bar{\varepsilon}_{\mathrm{rms}} = \sqrt{\frac{1}{N-1}\sum_{i=1}^{N-1}(\varepsilon_i - \bar{\varepsilon})^2}, \tag{17}$$

where N is the number of recorded images and ε_i is the i-th displacement value. The frequency spectrum of the silicone rod's displacement is estimated in two ways: by means of the Fast Fourier Transform (FFT) of whom an example is shown in Fig. 5c, and by evaluating the autocorrelation function of $\varepsilon(t)$ (Fig. 5a). The frequency at which periodical oscillation of the rod occurred is revealed by a peak. The Bartlett's method is applied to reduce the noise in the spectra (Monson, 1996). The peak in the spectrum obtained evaluating the autocorrelation function is fitted with a Gaussian bell to obtain a mean value of the frequency (Fig. 5b). The fitting error is calculated as the Normalised Root Mean Square Error (NRMSE):

$$\mathrm{NRMSE} = \frac{\sqrt{\frac{1}{N_s}\sum(x_{\mathrm{fit}} - x_s)^2}}{\bar{x}_s}, \tag{18}$$

where N_s is the number of fitted points of the peak, and x_{fit} and x_s are the fitted and the measured value of the spectrum, respectively. The frequency interval where fitting the spectral peak is chosen based on where the peak's first derivative nullifies. The accuracy with which the average frequency is determined is lower than 2%. For each flow rate $\bar{\varepsilon}$, $\bar{\varepsilon}_{\mathrm{rms}}$, and the corresponding frequency of vibration are calculated. The noise in the signal, estimated through a no-flow recording, corresponds to an equivalent displacement of 3μ m (the minimum measurable displacement is 9μ m). The time signal of the displacement is finally filtered with a Henderson's 23 points moving average to reduce such a noise (Cioncolini et al., 2018).

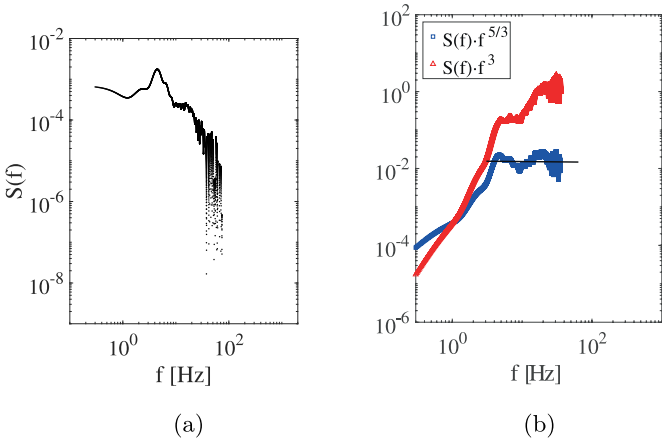

Fig. 6. (a) Frequency spectrum calculated at the centre of the gap. (b) $S(f)\cdot f^{5/3}$ (blue square), $S(f)\cdot f^{3}$ (red triangle). Re_e= 12 730. The black line highlights a plateau, indicating 3-dimensional turbulence. (For interpretation of the references to colour in this figure legend, the reader is referred to the web version of this article.)

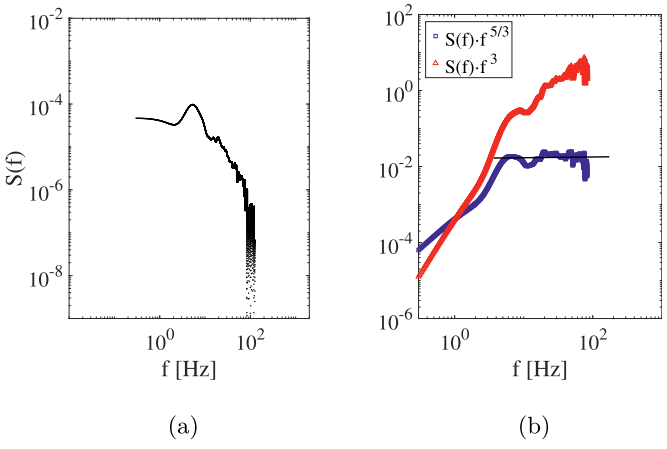

Fig. 7. (a) Frequency spectrum calculated at the centre of the gap. (b) $S(f)\cdot f^{5/3}$ (blue square), $S(f)\cdot f^{3}$ (red triangle). Re_e=14 950. The black line highlights a plateau, indicating 3-dimensional turbulence. (For interpretation of the references to colour in this figure legend, the reader is referred to the web version of this article.)

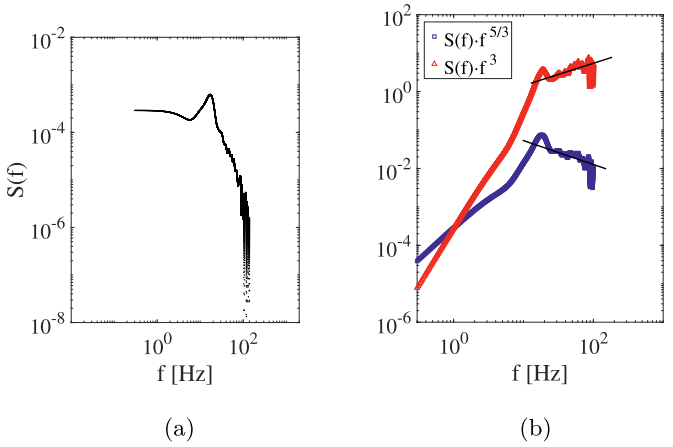

Fig. 8. (a) Frequency spectrum calculated at the centre of the gap. (b) $S(f)\cdot f^{5/3}$ (blue square), $S(f)\cdot f^{3}$ (red triangle). Re_e = 48 630. The black line highlights a plateau, indicating 3-dimensional turbulence. (For interpretation of the references to colour in this figure legend, the reader is referred to the web version of this article.)

5. Results and discussion

This section presents the results of the measurements: the first part characterises the coherent structures occurring in the flow and presents the new empirical correlation to estimate their wavelength. The second part reports the results of the measurements with the high-speed camera of fluid-structure interactions, focusing on the influence of coherent structures on the oscillation of the rod wall.

5.1. Coherent structures

Spectral analysis is performed on the stream-wise velocity component measured with the help of LDA. The turbulence inside the gap between the two front rods is examined based on the corresponding turbulence spectrum. This analysis is based on the slope of the spectrum: it helps to assess whether turbulence is two-dimensional or three-dimensional (2D, 3D for short) within the inertial subrange of the spectrum. Then this section will focus on the wavelength and the frequency of the coherent structures. The wavelength is used to validate an empirical correlation as proposed in Section 5.2.1, while the measured frequency of passage of the coherent structures is compared with the structural response frequency of vibration of the rod wall, as discussed in Section 5.3.

5.1.1. Characterising turbulence

The analysis of the frequency spectrum of the velocity helps to characterise turbulence by looking at whether the turbulence is 2D or 3D. For a 3D homogeneous turbulent flow, only the energy conservation equation applies and the inertial subrange of the turbulent spectrum usually shows the well-known slope of $-5/3$. In 2D turbulence the vortex-stretching effect is absent (Batchelor, 1969), hence the general vorticity equation for incompressible and inviscid fluid takes the form

$$\frac{D\omega}{Dt} = 0, \tag{19}$$

where $\frac{D\cdot}{Dt}$ is the lagrangian (or substantial) derivative. Eq. (19) expresses the conservation of vorticity. This is a second conservation equation that changes the slope of the spectrum from $-5/3$ to -3, within the inertial subrange. The energy cascade moves towards larger scales (lower wavenumber), and vorticity transfers to the smallest scales in the viscous subrange, contrary to 3D turbulent flows (Kraichnan, 1967). The slope of the inertial subrange gives, thus, an indication of the type of turbulence. The frequency spectrum of the stream-wise velocity is evaluated in the middle of the gap between the edge and central subchannel. The frequency spectrum is multiplied by f^3 (or $f^{5/3}$): the resulting function $S(f)\cdot f^3$ (or $S(f)\cdot f^{5/3}$) should have, thus, a flat plateau within the frequency range where turbulence is 2D (or 3D) (Romano, 1995).

The plots of Fig. 6 refer to Re_e= 12 730 (Re_c= 9 560). Fig. 6a shows the frequency spectrum $S(f)$ and Fig. 6b shows both $S(f)\cdot f^3$ and $S(f)\cdot f^{5/3}$. A low-frequency peak is found, which is characteristic of coherent structures that affect periodically the velocity field while moving with the mean flow. Although the spectrum exhibits a -3 slope over a short frequency decade, the overall slope appears to close to -5/3, as shown by the almost flat plateau of the $S(f)\cdot f^{5/3}$ plot.

Fig. 7 reports the case with Re_e=14 950 (Re_c= 11 230), where the peak in the spectrum is at 5.3Hz. The slope of the spectrum is close to -5/3, as shown by the constant trend of $S(f)\cdot f^{5/3}$ in the same frequency range.

Fig. 8 refers to the case with Re_e= 48 630 (Re_c = 36 530), where coherent structures occur at a higher frequency, being 17Hz (Fig. 8a). The corresponding plots of $S(f)\cdot f^3$ and $S(f)\cdot f^{5/3}$ are shown in Fig. 8b. The spectrum at this Reynolds number has a slope between -3 and $-5/3$, meaning that the turbulent behaviour of the flow is intermediate between 2D and 3D: the flow is more anisotropic in the sense that two components are dominant over the third, contrarily to three-dimensional turbulence, where all the components are equally important.

5.2. Wavelength

For each flow rate, the turbulent spectra are evaluated along the path going from the edge to the central subchannel (Fig. 3b). The peaks found in the spectra reveal periodicities and the associated frequency f_{str} ascribed to structures occurring in the flow. The quantities in the following plots are rendered non dimensional. In particular, non dimensional frequencies f^* and non dimensional velocity v^* are defined as (Païdoussis, 2014):

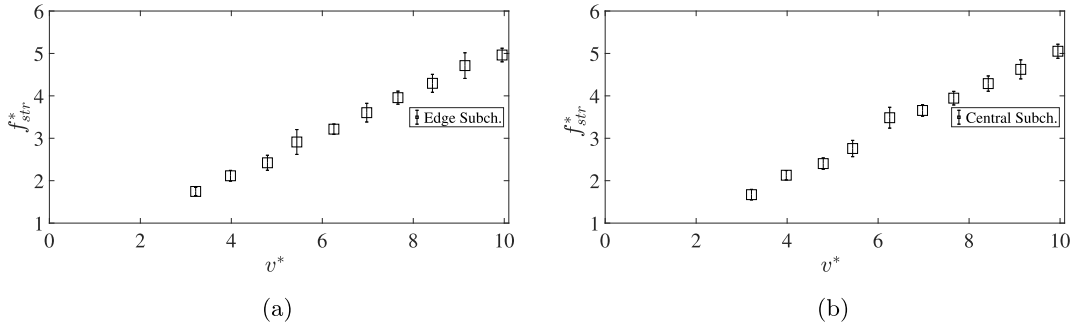

Fig. 9. Average frequency of passage of the coherent structures f_{str} against the non dimensional velocity v^*, measured (a) between the edge subchannel and the gap, and (b) between the gap and the central subchannel.

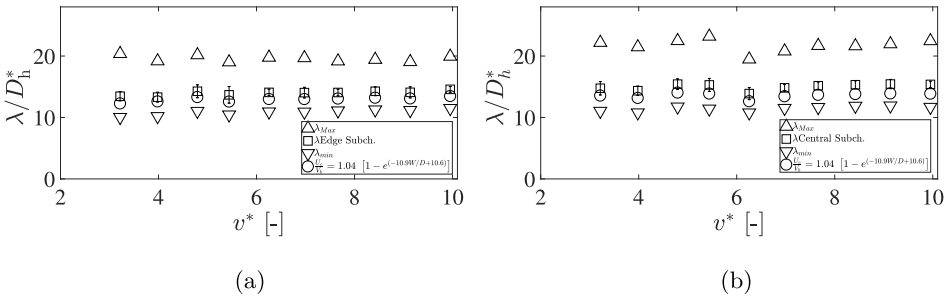

Fig. 10. Average non dimensional wavelength of the coherent structures λ/D_h^* depending on the non dimensional velocity v^*, measured (a) between the edge subchannel and the gap, and (b) between the gap and the central subchannel, where D_h^* is defined as in Fig. 1. (∘): Wavelength calculated using the empirical correlation for the convection speed of the structres provided in Guellouz and Tavoularis (2000).

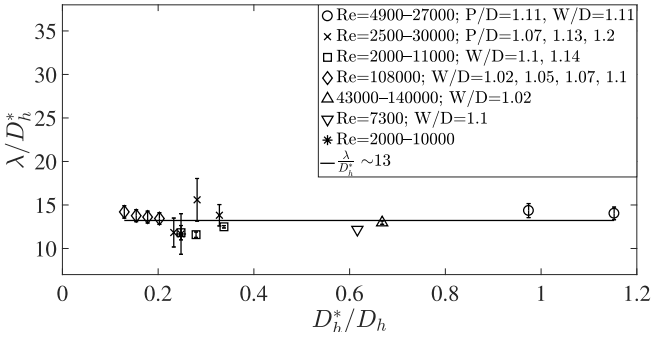

Fig. 11. Normalised structure wavelength λ/D_h^* against D_h^*/D_h. The Reynolds numbers in the legend are based on the total flow area of the test section. ∘: this work; × : data from Bertocchi et al. (2018); □: data from Mahmood (2011); ⋄: data from Guellouz and Tavoularis (2000); △: data from Don and Tavoularis (2018); ▽: data from Choueiri and Tavoularis (2014); * data from Lexmond et al. (2005).

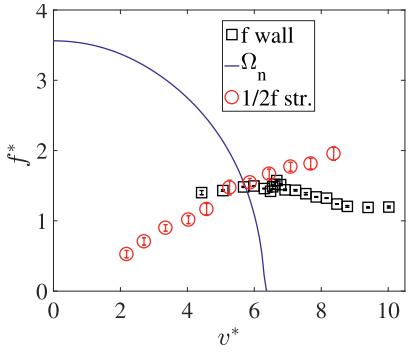

Fig. 12. Plot of $f_{str}/2$ (red circle), estimated natural frequency of the central silicone rod Ω_n (blue), and frequecy of vibration of the silicone rod wall f_{wall} (black square) measured with the high-speed camera. Frequencies are expressed as non-dimensional values. (For interpretation of the references to colour in this figure legend, the reader is referred to the web version of this article.)

$$f^* = f\,[\mathrm{Hz}]\cdot\sqrt{\frac{m + m_a}{EI}}L_{fl}^2; \qquad v^* = v\cdot\sqrt{\frac{m_a}{EI}}L_{fl}, \tag{20}$$

An average frequency of the structures is calculated based on the values given by the single peaks (Figs. 6–8). The plots of Fig. 9 report the average frequency f_{str} in both the edge and the central subchannel. The peaks in the frequency spectra show a bell-shaped distribution of frequencies. Namely, every peak is fitted with a Gaussian bell to obtain the corresponding standard deviation σ_{fit} around the mean. This gives a frequency interval $f_{str} \pm \sigma_{fit}$ which, in turn, provide a minimum and a maximum wavelength of the structures, as shown in Fig. 10. The NRMSE resulting from the fitting (Eq. (18)) is lower than 5% for all the considered cases. Taylor's hypothesis (coherent structures in the flow are regarded as frozen entities moving with the stream at velocity v_{in}) is adopted to obtain the wavelength of the structures. The velocity v_{in} is the stream-wise velocity measured at the inflection point of the profile between the gap and the subchannels (Mahmood, 2011). The average wavelength and its minimum and maximum values are

$$\lambda = \frac{v_{in}}{f_{str}}; \qquad \lambda_{Max} = \frac{v_{in}}{f_{str} - \sigma_{fit}}; \qquad \lambda_{min} = \frac{v_{in}}{f_{str} + \sigma_{fit}}. \tag{21}$$

The uncertainty on the wavelength λ is estimated from the uncertainty propagation formula as

$$\delta\lambda = \sqrt{\left(\frac{\partial\lambda}{\partial f_{str}}df_{str}\right)^2 + \left(\frac{\partial\lambda}{\partial v_{in}}dv_{in}\right)^2} \approx |\frac{\partial\lambda}{\partial f_{str}}df_{str}| = |\frac{v_{in}}{f_{str}^2}df_{str}|, \tag{22}$$

where the approximation is possible because the error on v_{in} is negligible compared to the uncertainty on f_{str}. The frequency at which the flow structures pass through the measurement region scales almost linearly with the flow velocity, suggesting that these keep a constant length independent of the Reynolds number. Fig. 10confirms that, at high Re_e, the average wavelength is independent of the Reynolds number, as shown by previous results (Bertocchi et al., 2018; Meyer and Rehme, 1995; Guellouz and Tavoularis, 2000; Mahmood, 2011).

The object of the next section will be the influence of the geometry of the channel over the structure's wavelength.

5.2.1. Empirical correlation validation

The normalised wavelength of the structures λ/D_h^* is evaluated for different geometries, and the results are reported in Fig. 11 against the normalised hydraulic diameter of the gap region D_h^*/D_h. The figure suggests that λ/D_h^* is constant and approximately equal to

$$\frac{\lambda}{D_h^*} \approx 13, \tag{23}$$

The wavelength of the structures scales linearly with the hydraulic diameter of the gap region D_h^*. If λ/D_h^* is constant, the coefficients $\xi = \gamma = 0$ in Eq. (8). If one imagines to increase indefinitely the hydraulic diameter of the main subchannel D_h while keeping the gap region the same (D_h^* and Re_{gap}), the wavelength of the structures is not expected to change much. This means that at some point λ/D_h^* will not depend on $(D_h^*/D_h)^\xi$, so it is reasonable to assume that

$$\xi = 0 \quad \text{for} \quad \frac{D_h^*}{D_h} \lesssim 1. \tag{24}$$

We see that the correlation is valid even for $D_h^*/D_h = 1.15$, which is the case of the near wall subchannel of the hexagonal bundle of this work (Fig. 1f). For a bundle, $D_h^*/D_h \lesssim 1$ means that the rod are moved farther. For the hexagonal bundle this ratio has a non-zero upper limit that is reached when the rods are in contact with each other (P/D = 1): D_h^*/D_h is 2.7 and 1.6 for the central and the edge subchannel, respectively. Obviously, this case falls out of the scope of this work as the

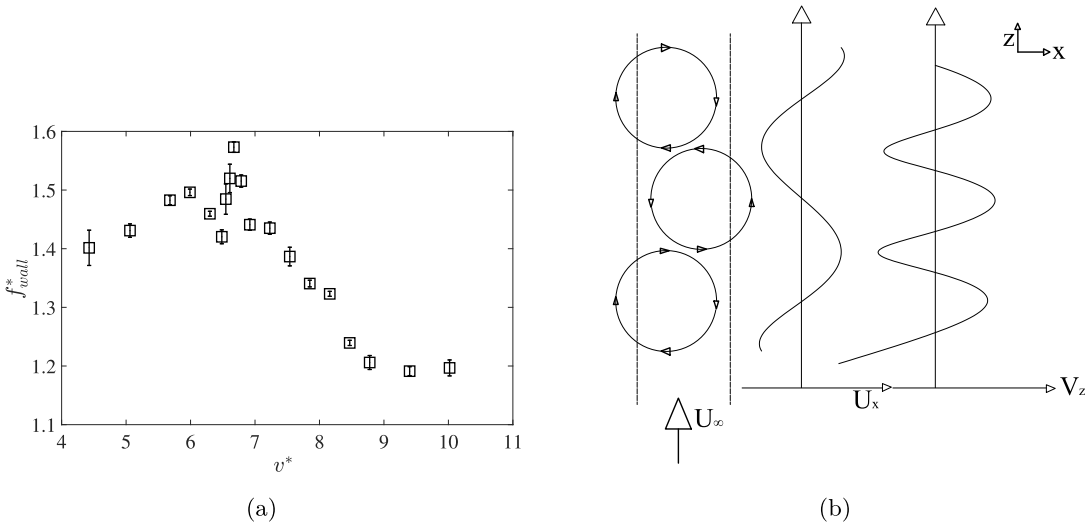

Fig. 13. (a) Non dimensional response frequency of the rod, depending on the non dimensional velocity v^*. (b) Gap vortex streets moving with the axial flow along a gap, identified by the dashed borders; originally proposed by Meyer and Rehme (1994).

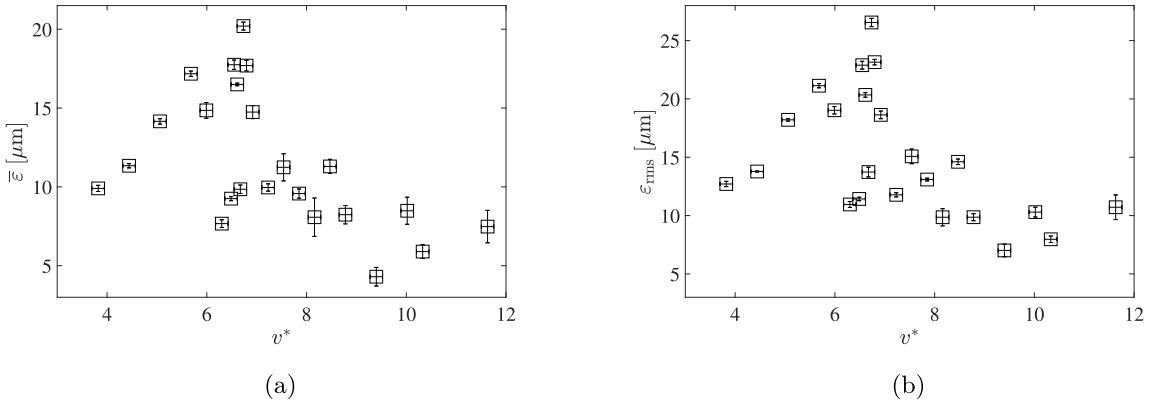

Fig. 14. Average displacements of the silicone rod border (a) and displacement root mean square (b) depending on the Reynolds. A clear peak in both plots, once compared with the measured response frequency, indicates synchronisation between the rod and the flow structures.

contact between the rods would damage the fuel elements of a nuclear reactor. The experiment performed with an eccentric rod inside a circular channel (Choueiri and Tavoularis, 2014) are also included in the plot (▽ in Fig. 11). Nevertheless, it deserves special care due to the much different geometry than a bundle since the borders of the gap region are not clearly identifiable.

5.2.2. Concluding remarks on coherent structures

Coherent structures are detected inside edge and central subchannels, as well as inside the interconnecting gap. Their frequency scales linearly with the flow rate, and the wavelength is not dependent on the Reynolds number. The wavelength of the coherent structures appears to scale linearly with the hydraulic diameter of the gap region of the channel as $\lambda \approx 13\ D_h^*$.

5.3. Fluid-structure interaction

This section discusses the results of the fluid-structure interaction measurements. The average frequency of vibration of the silicone rod's wall, f_{wall}, the average displacement $\bar{\varepsilon}$, and the $\bar{\varepsilon}_{rms}$ are obtained with ten series of measurements for each value of the flow rate (see Section 4.3 for details). The stream-wise rate of passage of the coherent structures, measured with LDA in the central subchannel (Fig. 9b), is also used for the analysis. The natural frequency of the silicone rod is estimated depending on the local velocity around the central flexible rod (see Section 2.1 for details). The three series, made non dimensional, are plotted in Fig. 12.

The trend of f_{str} increases linearly, as discussed in Section 5.2. The natural frequency Ω_n decreases with the velocity of the surrounding fluid: as the flow increases, the damping action of the term $\frac{1}{2}C_N\frac{m_a U}{D}$ grows under the action of the flow confinement (Païdoussis, 1974), especially with highly confined flows with low P/D ratios. f_{wall} shows a nearly constant frequency for $Re_e \approx 29\,000$, and drops for higher Re_e numbers (Fig. 12 and more in detail in Fig. 13a). Fig. 12 shows that the frequency of the structures f_{str} approaches twice the natural frequency of the rod $2\Omega_n$, and that the measured frequency of oscillation of the rod wall f_{wall} matches Ω_n. Both trends of the mean displacement of the wall, $\bar{\varepsilon}$, and its root mean square, $\bar{\varepsilon}_{rms}$, (Fig. 14) display a clear peak in the Reynolds number range where $f_{str} = 2\Omega_n$ (Fig. 12). Fig. 12 can have the following interpretation. Choueiri and Tavoularis (2014) found that the lateral velocity component of the vortex street oscillated with half the rate of passage of the coherent structures in the axial direction $f_{str}/2$. This was consistent with Meyer and Rehme's model (sketched in Fig. 13b), and with the experiments reported in Païdoussis et al. (1980) for a pulsating flow. According to the model, the counter-rotating large coherent structures produce a fluctuating velocity field. Decomposing such a field along the span-wise and stream-wise directions x and z, gives a velocity that fluctuates twice as fast along the stream-wise direction (V_z in Fig. 13b). Conversely, the span-wise component (U_x in Fig. 13b) would oscillate twice as slow around the zero. This fluctuation

of the lateral velocity component would lead to an external force imposed on the rod, fluctuating in time with $f_{str}/2$. When such force oscillates with $f_{str}/2 = \Omega_n$ (shown in Fig. 12), the rod and the vortex street are synchronized with each other and the magnitude of the oscillations increases (Williamson and Govardhan, 2004), as shown in Fig. 14.

6. Conclusions

This work aimed at studying the structural response of the central rod to large coherent structures occurring in the flow through a hexagonal bundle of rod tightly clustered (P/D = 1.11). The flow was studied with LDA while the flow-induced vibrations on the rod were recorded with a high-speed camera. The optical accessibility to the measurement region was achieved by means of the RIM technique. The measurements of the frequency and the displacement showed the synchronization between the rod and the structures when these move with twice the natural frequency of the rod. This condition is characterised by the increased magnitude of the oscillations and by a response near to the natural frequency of the rod. A new correlation for estimating the wavelength of the structures is derived based on dimensional analysis and experiments, resulting in a wavelength that scales linearly with the hydraulic diameter of the gap region. The correlation is valid for different geometries, involving channels with single rods or more complex rod bundles with P/D (or W/D) ranging from 1.02 to 1.20. The findings of this work contribute to explain further the physics of the flow-induced vibrations of coherent structures arising in axial rod bundle flows, typical of industrial applications. Furthermore, the correlation that we propose may be helpful in designing industrial components that are not prone to resonance phenomena and, thus, mechanical fatigue.

Acknowledgements

This project has received funding from the Euratom research and training programme 2014–2018 under the grant agreement No. 654935.

The author would like to thank Ing. Dick de Haas and Ing. John Vlieland for the technical support provided during the work.

References

Adrian, R.J., Yao, C.S., 1986. Power spectra of fluid velocities measured by laser Doppler velocimetry. Exp. Fluids 5 (1), 17–28. https://doi.org/10.1007/BF00272419.

Baratto, F., Bailey, S.C.C., Tavoularis, S., 2006. Measurements of frequencies and spatial correlations of coherent structures in rod bundle flows. Nucl. Eng. Des. 236 (17), 1830–1837. https://doi.org/10.1016/j.nucengdes.2005.12.009.

Batchelor, G.K., 1969. Computation of the energy spectrum in homogeneous two-dimensional turbulence. Phys. Fluids 12 (12), II–233. https://doi.org/10.1063/1.1692443.

Bertocchi, F., Rohde, M., Kloosterman, J.L., 2018. LDA measurements of coherent flow structures and cross- flow across the gap of a compound channel with two half-rods. Nucl. Eng. Des. 326, 17–30. https://doi.org/10.1016/j.nucengdes.2017.10.023.

Chang, D., Tavoularis, S., 2005. Unsteady numerical simulations of turbulence and coherent structures in axial flow near a narrow gap. J. Fluids Eng. 127 (3), 458. https://doi.org/10.1115/1.1900140.

Chen, S.K., Chen, Y.M., Todreas, N.M., 2018. The upgraded Cheng and Todreas correlation for pressure drop in hexagonal wire-wrapped rod bundles. Nucl. Eng. Des. 335, 356–373. https://doi.org/10.1016/j.nucengdes.2018.05.010.

Chen, S.S., 1985. Flow - Induced Vibration of circular cylindrical structures. Report ANL-85-51. Argonne National Laboratory, Argonne (IL).

Choueiri, G.H., Tavoularis, S., 2014. Experimental investigation of flow development and gap vortex street in an eccentric annular channel. Part 1. Overview of the flow structure. J. Fluid Mech. 752 (2014), 521–542. https://doi.org/10.1017/jfm.2014.343.

Choueiri, G.H., Tavoularis, S., 2015. Experimental investigation of flow development and gap vortex street in an eccentric annular channel. Part 2.Effects of inlet conditions, diameter ratio, eccentricity and Reynolds number. J. Fluid Mech. 768 (2015), 294–315. https://doi.org/10.1017/jfm.2015.90.

Cioncolini, A., Silva-Leon, J., Cooper, D., Quinn, M.K., Iacovides, H., 2018. Axial-flow-induced vibration experiments on cantilever rods for nuclear reactor applications. Nucl. Eng. Des. 338, 102–118. https://doi.org/10.1016/j.nucengdes.2018.08.010.

Dominguez-Ontiveros, E.E., Hassan, Y., 2009. Non-intrusive experimental investigation of flow behavior inside a 5 × 5 rod bundle with spacer grids using PIV and MIR. Nucl. Eng. Des. 239, 888–898. https://doi.org/10.1016/j.nucengdes.2009.01.009.

Dominguez-Ontiveros, E.E., Hassin, Y., 2014. Experimental study of a simplified 3 × 3 rod bundle using DPTV. Nucl. Eng. Des. 279, 50–59. https://doi.org/10.1016/j.nucengdes.2014.04.037.

Don, A., Tavoularis, S., 2018. Measurements of turbulent flow in a large-scale model of a 37-rod bundle. Nucl. Eng. Des. 337, 116–127. https://doi.org/10.1016/j.nucengdes.2018.06.018.

Gosset, A., Tavoularis, S., 2006. Laminar flow instability in a rectangular channel with a cylindrical core. Phys. Fluids 18 (4). https://doi.org/10.1063/1.2194968.

Guellouz, M.S., Tavoularis, S., 2000. The structure of turbulent flow in a rectangular channel containing a cylindrical rod - Part 1: Reynolds-averaged measurements. Exp. Therm. Fluid Sci. 23 (1–2), 59–73. https://doi.org/10.1016/S0894-1777(00)00038-8.

Hoerner, S.F., 1965. Fluid-Dynamic Drag. Hoerner Fluid Dynamics, Bakersfield, CA (US).

Hosokawa, S., Yamamoto, T., Okajima, J., Tomiyama, A., 2012. Measurements of turbulent flows in a 2 × 2 rod bundle. Nucl. Eng. Des. 249, 2–13. https://doi.org/10.1016/j.nucengdes.2011.11.035.

Idel'chik, I.E., 1966. Handbook of Hydraulic Resistance. Israel Program for Scientific Translations.

Kraichnan, R.H., 1967. Inertial ranges in two-dimensional turbulence. Phys. Fluids 10 (7), 1417–1423. https://doi.org/10.1063/1.1762301.

Larchevêque, M., 1993. Pressure field, vorticity field, and coherent structures in two-dimensional incompressible turbulent flows. Theor. Comput. Fluid Dyn. 5 (4–5), 215–222. https://doi.org/10.1007/BF00271659.

Lexmond, A.S., Mudde, R.F., Hagen, T.H.J.J.V.D., 2005. Visualisation of the vortex street and characterisation of the cross flow in the gap between two sub-channels. Proc. 11th International Topical Meeting on Nuclear Reactor Thermal-Hydraulics. Avignon, France

Mahmood, A., 2011. Single-Phase Crossflow Mixing in a Vertical Tube Bundle Geometry - An Experimental Study. Delft University of Technology.

Mayo, W.T., 1974. A discussion of limitations and extensions of power spectrum estimation with burst counter LDV systems. Proceedings of the Second International Workshop on Laser Velocimetry, Vol.1, pp 90–101.

Merzari, E., Ninokata, H., 2011. Proper orthogonal decomposition of the flow in a tight lattice rod-bundle. Nucl. Eng. Des. 241 (11), 4621–4632. https://doi.org/10.1016/j.nucengdes.2010.12.005.

Métais, O., Lesieur, M., 1992. Spectral large-eddy simulations of isotropic and stably stratified turbulence. J. Fluid Mech. 239, 157–194. https://doi.org/10.1017/S0022112092004361.

Meyer, L., 2010. From discovery to recognition of periodic large scale vortices in rod bundles as source of natural mixing between subchannels-A review. Nucl. Eng. Des. 240 (6), 1575–1588. https://doi.org/10.1016/j.nucengdes.2010.03.014.

Meyer, L., Rehme, K., 1994. Large-scale turbulence phenomena in compound rectangular channels. Exp. Therm. Fluid Sci. 8 (4), 286–304. https://doi.org/10.1016/0894-1777(94)90059-0.

Meyer, L., Rehme, K., 1995. Periodic vortices in flow through channels with longitudinal slots or fins. Tenth Symposioum on Turbulent shear flows. pp. 6.

Modarres-Sadeghi, Y., Païdoussis, M.P., Semler, C., Grinevich, E., 2008. Experiments on vertical slender flexible cylinders clamped at both ends and subjected to axial flow. Philos. Trans. Ser. A Math.Phys. Eng. Sci. 366 (1868), 1275–1296. https://doi.org/10.1098/rsta.2007.2131.

Möller, S.V., 1991. On phenomena of turbulent flow through rod bundles. Exp. Therm. Fluid Sci. 4 (1), 25–35. https://doi.org/10.1016/0894-1777(91)90018-M.

Monson, H.H., 1996. Statistical Digital Signal Processing and Modeling. John Wiley & Sons.

Nguyen, T., Goth, N., Jones, P., Lee, S., Vaghetto, R., Hassan, Y., 2017. PIV measurements of turbulent flows in a 61-pin wire-wrapped hexagonal fuel bundle. Int. J. Heat Fluid Flow 65, 47–59. https://doi.org/10.1016/j.ijheatfluidflow.2017.03.007.

Nguyen, T., Hassan, Y., 2017. Stereoscopic particle image velocimetry measurements of flow in a rod bundle with a spacer grid and mixing vanes at a low Reynolds number. Int. J. Heat Fluid Flow 67, 202–219. https://doi.org/10.1016/j.ijheatfluidflow.2017.08.011.

Nobach, H., 2002. Local time estimation for the slotted correlation function of randomly sampled LDA data. Exp. Fluids 32 (3), 337–345. https://doi.org/10.1007/s003480100362.

Okubo, A., 1970. Horizontal dispersion of floatable particles in the vicnity of velocity singularies such as convergences. Deep-sea Res. 17 (445–454), 445–454. https://doi.org/10.1016/0011-7471(70)90059-8.

Otsu, N., 1979. A threshold selection method from gray-level histograms. IEEE Trans. Syst. Man Cybern. 9, 62–66.

Païdoussis, M.P., 1966. Dynamics of flexible slender cylinders in axial flow Part 1. Theory. J. Fluid Mech. 26 (04), 717–736. https://doi.org/10.1017/S0022112066001484.

Païdoussis, M.P., 1974. The dynamical behaviour of cylindrical structures in axial flow. Ann. Nucl. Sci. Eng. 1 (2), 83–106. https://doi.org/10.1016/0302-2927(74)90055-5.

Païdoussis, M.P., 1981. Fluidelastic vibration of cylinder arrays in axial and cross flow: state of the art. J. Sound Vib. 76 (3), 329–360. https://doi.org/10.1016/0022-460X(81)90516-2.

Païdoussis, M.P., 2014. Fluid-Structure Interactions – Slender Structures and Axial Flow. 1 Elsevier.

Païdoussis, M.P., 2016. Fluid-Structure Interactions – Slender Structures and Axial Flow. 2 Elsevier.

Païdoussis, M.P., Issid, N.T., Tsui, M., 1980. Parametric resonance oscillations of flexible slender cylinders in harmonically perturbed axial flow. Part 2: experiments. J. Appl. Mech. 47, 715–719. https://doi.org/10.1115/1.3153779.

Pettigrew, M.J., Taylor, C.E., 1994. Two-phase flow-induced vibration: an overview. J. Pressure Vessel Technol. Trans. ASME 116 (3), 233–253. https://doi.org/10.1115/1.

2929583.
Piot, E., Tavoularis, S., 2011. Gap instability of laminar flows in eccentric annular channels. Nucl. Eng. Des. 241 (11), 4615–4620. https://doi.org/10.1016/j.nucengdes.2010.08.025.
Pope, S.B., 2000. Turbulent Flows. Cambridge University Press, Cambridge (UK).
Rayleigh, L., 1879. On the stability, or instability, of certain fluid motions. Proc. London Math. Soc. s1-11 (1), 57–72.
Rehme, K., 1987. The structure of turbulent flow through rod bundles. Nucl. Eng. Des. 99 (C), 141–154. https://doi.org/10.1016/0029-5493(87)90116-6.
Ridder, J.D., Degroote, J., Tichelen, K.V., Vierendeels, J., 2016. Vortex-induced vibrations by axial flow in a bundle of cylinders, Extended summary. International Conference on Flow-Induced Vibrations.
Romano, G.P., 1995. Analysis of two-point velocity measurements in near-wall flows. Exp. Fluids 20 (2), 68–83. https://doi.org/10.1007/BF00189296.
Rowe, D.S., Johnson, B.M., Knudsen, J.G., 1974. Implications concerning rod bundle crossflow mixing based on measurements of turbulent flow structure. Int. J. Heat Mass Transfer 17 (3), 407–419. https://doi.org/10.1016/0017-9310(74)90012-X.
Sato, H., Kobayashi, J., Miyakoshi, H., Kamide, H., 2009. Study on velocity field in a wire wrapped fuel pin bundle of sodium cooled reactor-detailed velocity distribution in a subchannel. 13th International Topical Meeting on Nuclear Reactor Thermal Hydraulics (NURETH-13). Kanazawa City, Japan
Sinyavskii, V.F., Fedotovskii, V.S., Kukhtin, A.B., 1980. Oscillation of a cylinder in a viscous liquid. Prikladnaya Mekhanika 16, 62–67.
Tavoularis, S., 2011. Reprint of: rod bundle vortex networks, gap vortex streets, and gap instability: a nomenclature and some comments on available methodologies. Nucl. Eng. Des. 241 (11), 4612–4614. https://doi.org/10.1016/j.nucengdes.2011.09.043.
Todreas, N.E., Kazimi, M.S., 1990. Nuclear Systems I: Thermal Hydraulic Fundamentals. Vol. 1. Taylor & Francis.
Tummers, M.J., Passchier, D.M., 1996. Spectral analysis of Individual Realization LDA data. Technical Report. Delft University of Technology, Faculty of Aerospace Engineering, Report LR 808.
Tummers, M.J., Passchier, D.M., 2001. Spectral analysis of biased LDA data. Meas. Sci. Technol. 12 (10), 1641–1650. https://doi.org/10.1088/0957-0233/12/10/304.
Weiss, J., 1991. The dynamics of enstropy transfer in 2-dimensional hydrody00namics. Physica D 48, 273.
White, F.M., 2016. Fluid Mechanics, (8th ed.). Mc Graw Hill.
Williamson, C.H.K., Govardhan, R., 2004. Vortex-induced vibrations. Annu. Rev. Fluid Mech. 36 (1), 413–455. https://doi.org/10.1146/annurev.fluid.36.050802.122128.